Bioelectromagnetics 41:3–20 (2020)

Review

Wireless Wearables and Implants: A Dosimetry Review

Katrina Guido ,* and Asimina Kiourti

ElectroScience Laboratory, Department of Electrical and Computer Engineering, The Ohio State University, Columbus, Ohio

Wireless wearable and implantable devices are continuing to grow in popularity, and as this growth occurs, so too does the need to consider the safety of such devices. Wearable and implantable devices require the transmitting and receiving of electromagnetic waves near and through the body, which at high enough exposure levels may damage proximate tissues. The specific absorption rate (SAR) is the quantity commonly used to enumerate exposure levels, and various national and international organizations have defined regulations limiting exposure to ensure safe operation. In this paper, we comprehensively review dosimetric studies reported in the literature up to the year 2019 for wearables and implants. We discuss antenna designs for wearables and implants as they relate to SAR values and field and thermal distributions in tissue, present designs that have made steps to reduce SAR, and then review SAR considerations as they relate to applied devices. As compared with previous review papers, this paper is the first review to focus on dosimetry aspects relative to wearable and implantable devices. Bioelectromagnetics. 2020;41:3–20. © 2019 The Authors. *Bioelectromagnetics* published by Wiley Periodicals, Inc.

Keywords: SAR; antennas; thermal distribution; implantable devices; wearable devices

INTRODUCTION

Wireless wearable and implantable devices are becoming increasingly vital within many fields from health and fitness to video game development. Wearable devices already accompany an estimated 27% of Americans [Kiourti and Nikita, 2017], taking the form of everything from watches to glasses to socks, and are used to track the wearer's vital signs, movement, location, surroundings, caloric expenditure, and sleep, among other information [Fernandez et al., 2018; Karthik and Rao, 2018]. Implantable devices are more invasive, usually requiring surgery, but can access information such as neural signals, not readily available to sensors externally placed to the body. In the medical field, wearable and implantable devices are used in the diagnosis, monitoring, and treatment of various illnesses and diseases. For example, cardiac pacemakers are used to monitor and treat heart disease, deep brain stimulators treat movement disorders and seizures associated with Parkinson's and epilepsy, respectively, hearing aids assist those with hearing loss, and smartwatches monitor trends in vital signs [Grant et al., 2004; Gwechenberger et al., 2006; Song et al., 2009; Kiourti et al., 2014; Ruaro et al., 2016]

With increased use and importance, an increased research interest into the electromagnetic (EM) safety of these devices has followed. Notably, the wireless nature of these devices requires the transmitting and receiving of EM radiation near and through the body, which can cause heating of and damage to body tissues due to the absorption of this energy [Chou et al., 1996; Chou and D'Andrea, 2003; Karthik and Rao, 2018; Kyriakou et al., 2012; Polikov et al., 2005; Wood and Karipidis, 2017]. Organizations such as the International Commission on Non-Ionizing Radiation Protection (ICNIRP), the Institute of Electrical and Electronics Engineers (IEEE), and the Federal Communications Commission (FCC) currently define safety limits for such EM exposure [FCC OET,

Conflicts of interest: None.

*Correspondence to: Katrina Guido, ElectroScience Laboratory, Department of Electrical and Computer Engineering, The Ohio State University, 1330 Kinnear Rd, Columbus, OH 43212; E-mail: guido.26@osu.edu

Received for review 16 May 2019; Accepted 4 December 2019

DOI:10.1002/bem.22240
Published online 18 December 2019 in Wiley Online Library (wileyonlinelibrary.com).

1997; ICNIRP, 1998; IEEE C95.1-2005, 2005]. Accordingly, EM safety in the wearables/implants literature is assessed in terms of specific absorption rate (SAR), tissue temperature increase, and related distributions, aiming to conform with national and international safety guidelines and to identify ways of safely increasing the transmitted power levels.

In this paper, we perform a thorough and comprehensive review of dosimetry studies reported in the literature up to the year 2019 for wearables and implants. Specifically, we begin by discussing antenna designs for wearables and implants as they relate to SAR values and field and thermal distributions in tissue, presenting designs that have made steps to reduce SAR, and then review SAR considerations as they relate to applied devices. As compared with other review papers, which have focused on antenna design [Kiourti, 2018], device power [Amar et al., 2015; Hinchet and Kim, 2015; Bandodkar, 2017], and sensor applications [Bergmann et al., 2012; Kiourti and Nikita, 2017; Koydemir and Ozcan, 2018], this paper is the first review to focus on dosimetry aspects related to wearable and implantable devices.

WEARABLES

Overview of Wearable Antenna Design

Wearable antennas may operate in one or both of on-body (in which the antenna communicates with other sensor nodes located on/in the body) or off-body (in which the antenna communicates with a device not worn on the body) communication modes [Xiaomu et al., 2017]. For example, Tong et al. [2018] designed a circular patch antenna of radius 24 mm with an omnidirectional radiation pattern for on-body communication and unidirectional radiation pattern for off-body communication. The patch design is considered low profile enough for body-worn applications. In addition to the microstrip patch antenna, various other types of antennas, such as vertical monopole, planar microstrip monopole, inverted-F, cavity-backed slot, and reflector patch, have been considered for wearable use [Jiang et al., 2014]. However, not all designs are suitable for body-worn applications, and even those that are low profile may be too large for certain applications/locations on the body. To maintain a lightweight and inconspicuous design, many wearable antennas are integrated into clothing [Agneessens et al., 2015]. Several of these textile antennas utilize conductive threads to stitch the antenna design onto the textile substrate, maintaining flexibility and allowing the antenna to conform to the wearer's body [Alharbi et al., 2018]. In other cases, metalized fabrics or conductive inks have been used for textile antennas [Scarpello et al., 2012]. The flexibility adds an additional layer of complexity, as bending of the antenna can affect the resonance. Ashyap et al. [2017] presented an inverse E-shaped microstrip monopole antenna $30 \times 20 \times 0.7\,\text{mm}^3$ made out of a denim substrate and ShieldIt Superconductive textile, whose resonance frequency did not shift with flexing.

Dosimetry for Wearable Antennas

SAR values. In addition to ensuring a wearable antenna's ability to be inconspicuous on the body, the safety of the antenna must be considered during the design process. The SAR values for various designs are shown in Table 1. SAR is calculated by averaging over a sample volume, generally 1 or 10 g with maximum general exposure limited to 1.6 W/kg ($SAR_{1\,g}$) or 2 W/kg ($SAR_{10\,g}$) by the FCC and the ICNIRP/International Electrotechnical Commission (IEC), respectively. For the same antenna and simulation setup, the maximum SAR obtained by averaging over 10 g is typically lower than that obtained by averaging over 1 g, as is seen in Table 1. SAR is determined via finite element analysis, method of moments, or finite-difference time-domain simulations and/or experimentally by using an electric field probe and performing the respective calculation, among other methods. Input power is commonly set to 0.1 or 0.5 W, as is seen in Table 1, the result of which can then be used to determine what input power level results in safe exposure levels if the resulting SAR is greater than allowed by regulation; however, some groups choose to determine the maximum possible input power allowed within safe SAR limits (e.g., Tong et al. [2018]). Different groups choose different phantoms/tissue models (e.g., rectangular prism of tissue versus a human head phantom), different sized phantoms, different tissue compositions, and different separations between the antenna and the phantom, which alter the SAR values. Some of the antennas presented in Table 1 are simulated in varying situations (i.e., antenna-phantom separations, etc.), and the values listed are from the worst-case scenario given in the respective paper. The corresponding setup description is provided briefly in Table 1.

Comparing Yan and Vandenbosch's [2016] patch antenna with Zhang et al.'s [2017a] patch antenna listed in Table 1, both of similar size, operating frequency, and phantom setup, the patch antennas exhibit similar SAR, though feeding via aperture-coupling results in an increased SAR despite the antenna being located twice as far from the phantom. Yan et al.'s [2015b] magneto-electric dipole, which is

TABLE 1. Comparison of Various Wearable Antennas and Their Corresponding Specific Absorption Rate (SAR) Values

Source	Antenna design	Size	Operation frequency	Input power for SAR calculation (mW)	$SAR_{1\,g}$ (W/kg)	$SAR_{10\,g}$ (W/kg)	SAR normalized to 1 W input power, 1 g; 10 g	Phantom type and distance to antenna
Zhang et al. [2017b]	Dual-mode button (spiral inverted-F)	18 mm radius	2.45/5.8 GHz	100	0.390/0.584	0.206/ 0.232	3.9/5.84; 2.06/2.32	2 mm gap, single-layer homogenous phantom $200 \times 130 \times 80\ mm^3$
Jiang et al. [2016]	Circularly polarized filtering patch	$55 \times 55 \times 5.2\ mm^3$	2.4 GHz	100	<0.54	–	<5.4; –	Numerical 3D volumetric HUGO body model, gap not specified
Agneessens et al. [2015]	Substrate integrate waveguide (SIW)	$\sim 60 \times 60\ mm^2$	2.4 GHz	500	0.45	–	0.9; –	2 mm gap, three-layer rectangular phantom (1 mm skin, 3 mm fat, 18 mm muscle depths)
Wang et al. [2013]	Shorted patch	$250 \times 250\ mm^2$	430 MHz	1,000	0.05	–	0.05; –	Environment described by IEEE 1528 standard, gap not specified
Tong et al. [2018]	Switchable patch	24 mm radius	2.45 GHz	108.2	1.6	–	14.79; –	5 mm gap, three-layer $100 \times 100\ mm^2$ rectangular phantom (1 mm skin, 2 mm fat, 10 mm muscle depths)
Zhang et al. [2017a]	Aperture-coupled patch	$100 \times 100 \times 3\ mm^3$	2.45 GHz	500	–	0.145	–; 0.29	10 mm gap, three-layer rectangular phantom (3 mm skin, 7 mm fat, 60 mm muscle depths)
Mandal and Pattnaik [2018]	Aperture	$70 \times 70\ mm^2$	1.8/2.4/3.6/5.5 GHz	500	–	0.121/ 0.411/ 0.566/ 0.798	–; 0.242/ 0.822/ 1.132/1.596	5 mm gap, three-layer $120 \times 120\ mm^2$ rectangular phantom (3 mm skin, 13 mm fat, 60 mm muscle depths)
Yan and Vandenbosch [2016]	Pattern-reconfigurable patch	$100 \times 100 \times 3.34\ mm^3$	2.4 GHz	500	–	0.05	–; 0.1	5 mm gap, three-layer $300 \times 300\ mm^2$ rectangular phantom (3 mm skin, 7 mm fat, 60 mm muscle depths)
Sundarsingh et al., [2014]	Slotted patch	$240 \times 240\ mm^2$	900/1800 MHz	–	–	0.00066/ 0.00237	–	$0.01\lambda_0$ gap, three-layer rectangular phantom (0.4 mm skin, 30 mm fat, 69.6 mm muscle depths)
Yan et al. [2015a]	Metamaterial-inspired slotted patch	$50 \times 50\ mm^2$	2.4/5.2 GHz	500	–	0.37/0.69	–; 0.74/1.38	5 mm gap, HUGO body model

(*Continued*)

TABLE 1. *Continued*

Source	Antenna design	Size	Operation frequency	Input power for SAR calculation (mW)	$SAR_{1\,g}$ (W/kg)	$SAR_{10\,g}$ (W/kg)	SAR normalized to 1 W input power, 1 g; 10 g	Phantom type and distance to antenna
Yan et al. [2015b]	Magneto-electric dipole	$100 \times 100 \times 6\ mm^3$	2.45/5 GHz	500	–	0.044/0.026	–; 0.088/0.052	6 mm gap, three-layer $300 \times 300\ mm^2$ rectangular phantom (3 mm skin, 7 mm fat, 60 mm muscle depths)
Fernandez et al. [2018]	Slotted monopole	$56 \times 33 \times 11\ mm^3$	2.45 GHz	100	–	0.316	–; 3.16	0 mm gap, voxel body model

also of similar size, operating frequency, and phantom to the patch antennas, exhibits a lower SAR value than either of the patch antennas. Anguera et al. [2012] compared the operation of a dipole, slot, loop, and patch antenna within the 2.4–2.5 GHz band on a homogenous human head phantom and found that although the dipole, loop, and slot antennas performed better in free space, the patch antenna offered the highest efficiency and lowest SAR once placed on the body. Again referring to Table 1, the multiband antennas tend to exhibit higher values of SAR at higher frequency bands, and of the compared patch antennas, those operating at lower frequencies generally exhibit lower SAR values.

However, SAR values are dependent on the environment in which the antenna is operating as well as the antenna type and specific geometry, so generalized conclusions cannot necessarily be derived by reviewing the literature, but rather such conclusions are application-specific. As such, in the following sections, we summarize findings wherever possible and to the most extent possible.

SAR and field distributions. As SAR is proportional to the square of the electric field, analysis of the field distribution on the antenna and within the body can indicate the SAR distribution. Blauert and Kiourti [2018] presented an antenna designed to match the permittivity of the human body across the 1–9 GHz frequency band. By using a horn antenna filled with cylindrical channels of distilled water, the permittivity of the horn will vary similarly to that of human tissue with varying frequency (human tissue is composed of a high percentage of water), thus increasing the impedance bandwidth of a typical horn antenna. The electric field of the antenna radiating at 2.4 GHz into a tissue-emulating phantom is shown in Figure 1. The placement of the water channels allows normal propagation of the fields relative to the antenna, allowing deeper field propagation into tissue. The SAR averaged over 1 g for this setup is shown in Figure 2, where the maximum SAR is found at the location of the maximum electric field amplitude, which is directly below the antenna. The bio-matched antenna allows an input power up to 8.57 dBm to stay within the FCC SAR guidelines.

Yan and Vandenbosch [2018] designed a wideband antenna that looks like a button using characteristic mode theory. By locating the button with the radiating element (circular loaded patch antenna with complementary split-ring resonator [CSRR]) on the short edge or corner of the ground layer (conductive textile intended to be located underneath a person's clothing—i.e., the clothing is located between the

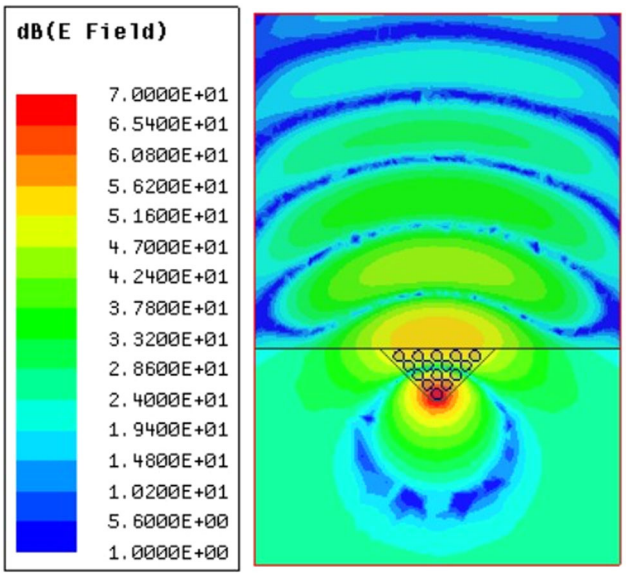

Fig. 1. Altering the antenna to match the characteristics of the human body into which the antenna is transmitting allows for lower specific absorption rate and better propagation into the body, as shown by the electric field distribution of a bio-matched antenna radiating at 2.4 GHz into a tissue-emulating phantom [Blauert and Kiourti, 2018].

button and ground plane), the impedance bandwidth is increased compared with other locations. Yan and Vandenbosch explain these locations as being optimal because the electric field is maximized at these locations, allowing for increased coupling to ground. This increased coupling excites additional modes in the conductive textile ground layer, increasing the bandwidth of the antenna. However, using the ground as a radiator increases SAR compared with other textile antennas, especially as the ground is brought closer to

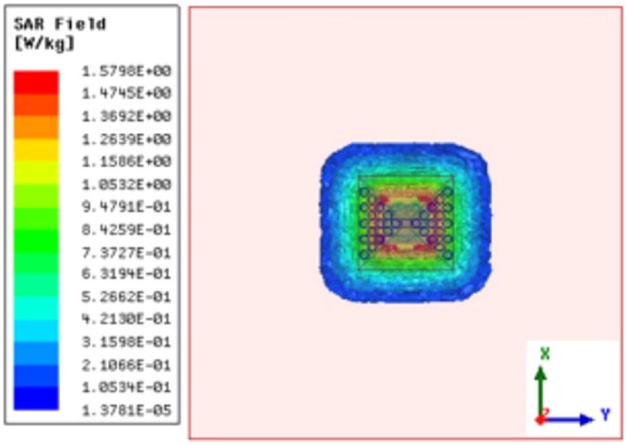

Fig. 2. Specific absorption rate (SAR_{1g}) for the setup described in Figure 1, where the maximum SAR in the phantom is found where the maximum electric field amplitude occurs [Blauert and Kiourti, 2018].

the body. Maximum SAR over 10 g for an input power of 15 dBm is still considered safe at 0.18 W/kg.

Simulated SAR distribution varies with location of the antenna on the body, among other factors, as tissue thickness and distribution vary across the body. Karthik and Rao [2018] noted that SAR values are lower in fat tissue than in deep muscle tissue due to fat tissue's lower water content (and therefore less energy absorption). They also noted that as the electric field is maximized just below their patch antenna, this area is where the highest levels of SAR occur, as is seen in Figures 3 and 4. Karthik and Rao also "observed that at greater GHz frequencies, reflections were increased due to reduced radiation absorption by the body. Hence, a decrease in SAR as frequency increases [Klemm and Troester, 2006] was noted." When modeling mobile phone usage with dipole antennas, Martínez-Búrdalo et al. [2009] additionally observed peak SAR levels occurring in the first few layers of body tissue closest to their antenna. To consider additional effects on SAR distribution, Martínez-Búrdalo et al. accounted for a person's surroundings, noting that these can also affect peak values—e.g., proximity to a brick wall may decrease SAR, whereas proximity to a metallic structure may increase SAR due to absorption and reflection of EM energy off of these surfaces, respectively, as is seen in Figure 5.

Mandal and Pattnaik [2018] observed that the surface area of the tissue model used to calculate SAR affects peak levels (larger surface areas decrease SAR by allowing increased diffusion of energy) while modeling a quad-band slot antenna. Acknowledging the aforementioned variations in SAR distribution, to determine optimal placement of their slot antenna design on the body, Fernandez et al. [2018] utilized a figure of merit F calculation. Plotting these results depicts the ratio of antenna efficiency to SAR for a single frequency for various antenna locations, allowing Fernandez et al. to determine that the left side of the torso results in the highest figure of merit (thus low SAR and high radiation efficiency) for their slot antenna.

Thermal distributions. The safety of the antenna is more dependent on the induced temperature change within the tissue than the power density value itself [Karthik and Rao, 2018]. However, as wearable device safety is typically characterized in terms of SAR, which is related to induced temperature changes, thermal effects of the antennas are not often considered. Karthik and Rao [2017] designed a multiband microstrip-based monopole for operation at 1.8, 2.4, 5.0, and 8.9 GHz and analyzed both the SAR and resulting thermal effects for various body locations. Simulations with

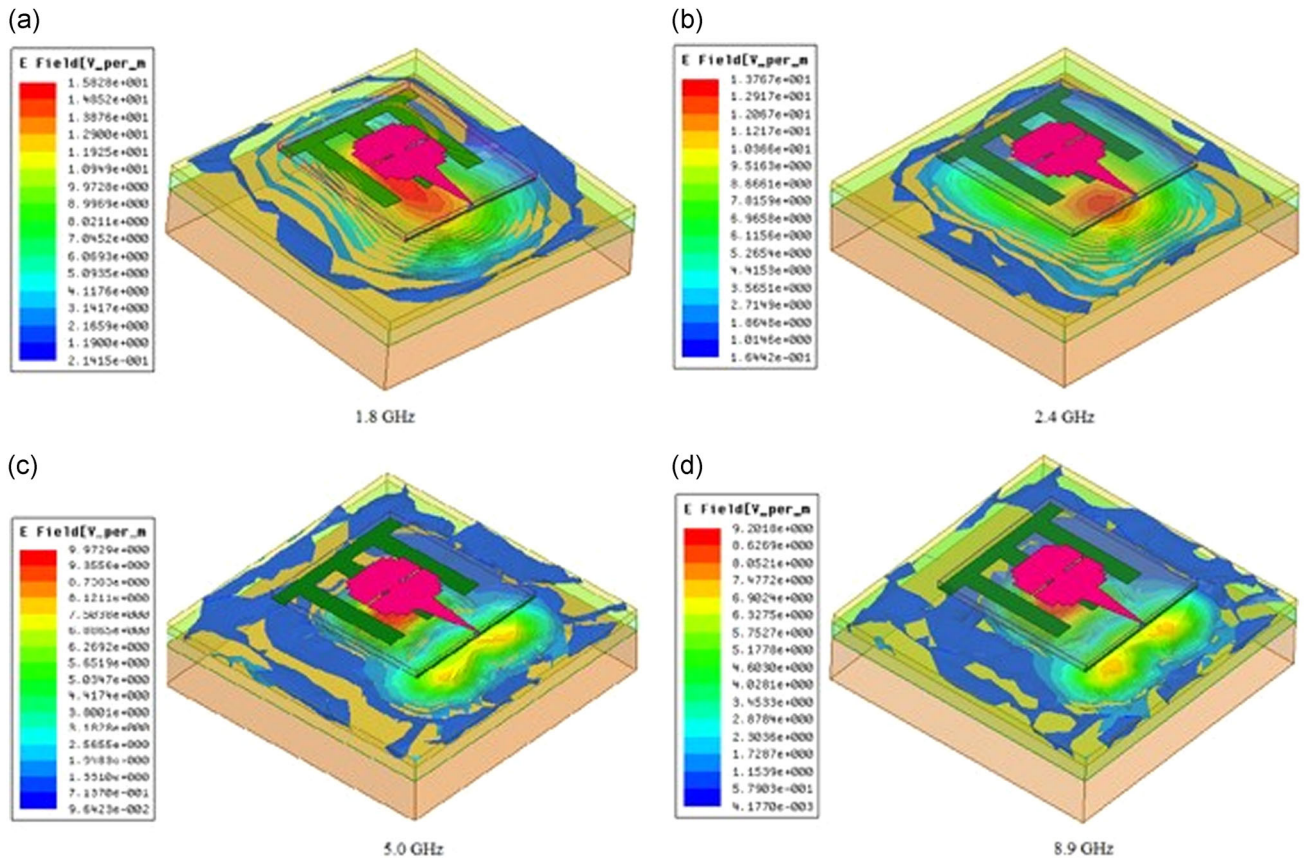

Fig. 3. Electric field distribution in the tissue of a patch antenna radiating at (a) 1.8 GHz, (b) 2.4 GHz, (c) 5.0 GHz, and (d) 8.9 GHz, with the highest field strength located directly below the patch [Karthik and Rao, 2018].

the monopole exhibited the highest SAR of 0.25 W/kg in the skin of the forearm at 1.8 GHz with the corresponding temperature increase of 0.15°C likewise being the largest. Verifying simulations via human trials with the antenna operating at 1.8 and 2.4 GHz on the forehead, wrist, and leg, and recording the temperature increase via an infrared (IR) camera, Karthik and Rao [2017] again found that the largest average temperature increase of 0.63 ± 0.23°C occurred at the wrist at 1.8 GHz. They further analyzed the evolution of the change in temperature over a 10^4 s period, noting that after less than half of the observation time (during which temperature increases) the temperature change reaches saturation due to the body's thermoregulation via blood flow.

Shrivastava and Rao [2017] tested a 60 GHz antipodal linear tapered slot antenna (ALTSA) exhibiting a SAR of 0.10 and 0.23 W/kg for a transmit power of 10 mW for operation near the head and anterior thigh, respectively. Recording the evolution of temperature, they noted that a maximum simulated and measured (using IR imaging) skin surface temperature increase of 0.82 and 0.6°C occurred, respectively, in the anterior thigh, and there was a maximum simulated and measured temperature increase of 0.52 and 0.4°C, respectively, in the head.

Manoufali et al. [2018] designed a wearable loop antenna for powering an implant via inductive coupling. Though simulations showed that most of the surrounding tissue temperatures stayed at the initial body temperature of 37°C with an input power of 1 W, the model exhibited a noticeable temperature increase at the skin layer directly below the antenna, with the skin having absorbed 14% of the incident power.

Reducing SAR Levels

Several techniques have been employed to ensure low SAR levels and to maintain high efficiency. Trajkovikj and Skrivervik [2015] note that antennas without a ground plane (e.g., a dipole) will exhibit higher SAR values as SAR of on-body antennas in part relies on near-field coupling to

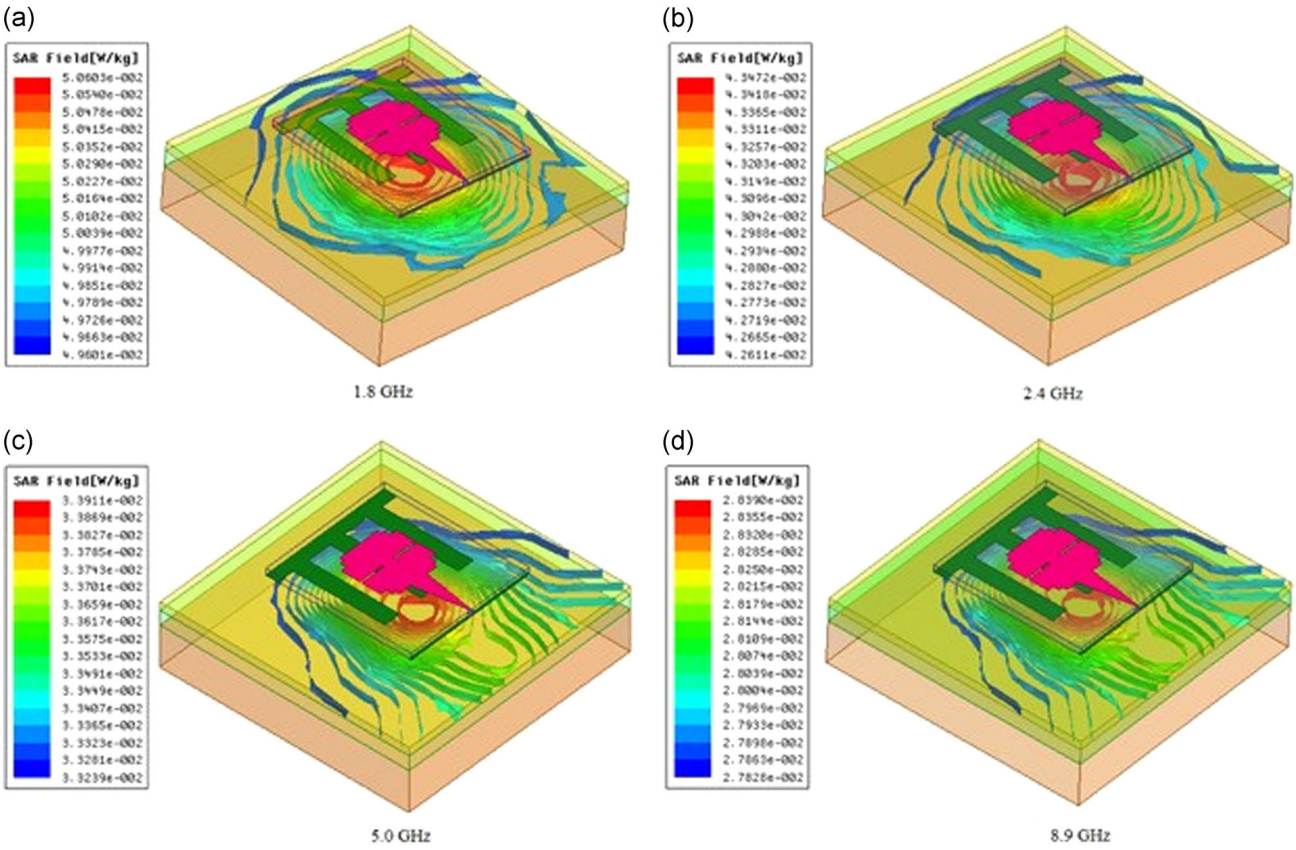

Fig. 4. Corresponding specific absorption rate ($SAR_{1\,g}$) distribution of the patch antenna shown in Figure 3, where the maximum SAR occurs at the location of the greatest maximum field amplitude for (a) 1.8 GHz, (b) 2.4 GHz, (c) 5.0 GHz, and (d) 8.9 GHz [Karthik and Rao, 2018].

the body. Thus, many of the methods to reduce SAR of off-body radiating antennas rely on altering the ground plane. One such technique is the use of electromagnetic bandgap (EBG) structures, or periodic conductive structures used to filter EM waves within certain frequency bands. Gao et al. [2018] utilized a rectangular ring-shaped EBG to reflect away from the body any radiation that the planar inverted-F antenna (PIFA) would normally direct toward the body. Their results demonstrated that at 2.45 GHz the PIFA without the EBG exhibited a maximum SAR over 1 g of 7.23 W/kg, while the PIFA with a 3×3 EBG geometry exhibited a maximum SAR of 0.972 W/kg. Adding an additional column to make a 3×4 EBG structure further decreased SAR over 1 g at 2.45 GHz to 0.0908 W/kg, dissipating electric field hot spots associated with the square array. Zhu and Langley [2009] found that adding a 3×3 EBG structure reduced the SAR of their coplanar textile antenna by up to 20 times, which they verified both via simulation and experiment with the DASY4 automated system. Similarly, Chen and Ku [2016] integrated a fractional factorial design high impedance surface (HIS) with an inverted-L antenna, which likewise blocks EM waves within a certain frequency band, prevents propagating surface waves, and reflects EM waves with no phase reversal. Without the HIS, SAR averaged over 1 g was 13.5 W/kg, but with the integrated 2×2 cross-shaped slot HIS, SAR dropped over 90% to 0.29 W/kg. Integrating an artificial magnetic conductor (AMC) ground plane also serves as an isolator. A dual-band, polarization-dependent AMC surface was used to reduce the maximum SAR over 1 g of a reconfigurable slot antenna from 2 to 0.29 W/kg [Saeed et al., 2017].

Additional ground plane structures can add bulk to an antenna, so Bhattacharjee et al. [2017] introduced a truncated ground plane to reduce electric field hot spots. Introducing a single-arm meander of the antenna near the feedline joined to an inverted ground section reduces hot spots, which are primarily focused near the antenna feed, without altering the feed itself. Additional SAR reduction techniques include the integration of ferrite sheets and metamaterials, and the aforementioned methods are compared in Table 2.

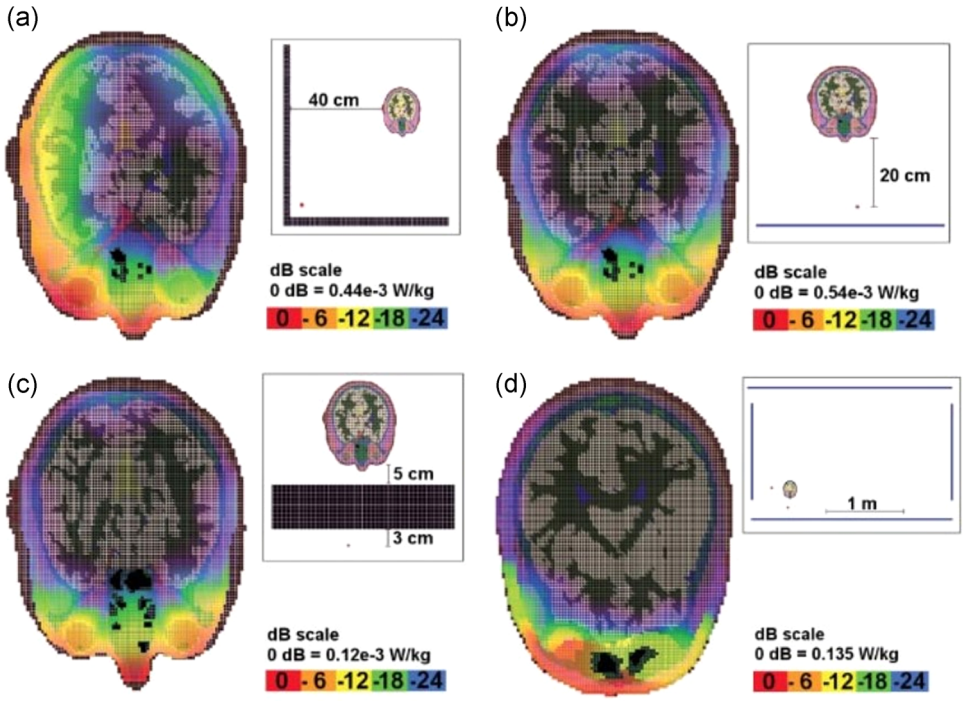

Fig. 5. Induced specific absorption rate (SAR) can vary based on a person's surroundings. $SAR_{10\,g}$ distribution of a human head with the antenna (**a**) 4 cm from two brick walls joined at a corner (**b**) 4 cm from a single metal wall (**c**) 3 cm on the opposite side of a 12 cm thick brick wall (**d**) and an additional antenna situated on metal cabinets [Martínez-Búrdalo et al., 2009].

Dosimetry for Integrated Wearable Devices

Once an antenna is integrated into a device, SAR values may change as new materials are integrated with the antenna [Hong et al., 2016a; Hong and Choi, 2018]. Fernández-Garcia and Gil [2017] created a textile-based wearable tracking system via a meandered inverted-F antenna integrated with a GPS receiver, microcontroller, SIGFOX transmitter, and battery. For operation at 868 MHz, simulated peak SAR values for operation on the thigh (i.e., integrated into pants) over 1 g for a male and female model were 0.619 and 0.998 W/kg,

TABLE 2. Comparison of Various Methods to Reduce Specific Absorption Rate (SAR)

Source	SAR reduction method	SAR without method (W/kg)	SAR with method (W/kg)	1 g or 10 g?	Input power (mW)	Frequency (GHz)
Jiang et al. [2014]	Metasurface	16.8	0.79	1	100	2.4
Agarwal et al. [2016]	AMC	34.3	1.81	1	1,000	2.45
Velan et al. [2015]	EBG	6.62	0.016	10	Not specified	2.45
Ashyap et al. [2017]	EBG	6.19	0.0368	1	100	2.4
Zhu and Langley [2009]	EBG	11.47	0.48	1	Not specified	1.8
Abirami and Sundarsingh [2017]	EBG	8.73	0.08	10	1,000	2.4
Gao et al. [2018]	EBG	7.23	0.972	1	Not specified	2.45
Chen and Ku [2016]	HIS	15	0.29	1	100	2.4
Saeed et al. [2017]	AMC	2	0.29	1	100	2.45, 3.3
Bhattacharjee et al. [2017]	Truncated ground plane	1.31	0.98	Not specified	Not specified	2.5
Augustine et al. [2010]	Polymeric ferrite sheet	13.12	1.44	1	250	2.4
Kwak et al. [2017]	AMC	1.023	0.58	10	316	1.97
Zhu and Langley [2009]	EBG	11.47	0.48	1	Not specified	1.8

AMC = artificial magnetic conductor; EBG = electromagnetic bandgap; HIS = high impedance surface.

respectively (the input power was not specified). When taken over 10 g, peak values for both the male and female models were 0.389 W/kg. Alkhamis et al. [2017] implemented a wearable tracking system as a wrist-wearable device, using a π-shaped antenna, for operation at 406 MHz and 1.5 GHz. The maximum SAR was focused at the gap of the feedline, affirming the same observation of Bhattacharjee et al. [2017], mentioned in Reducing SAR Levels.

Hong et al. [2016b] designed a transparent and flexible monopole antenna at 2.45 GHz for integration into smart glasses and analyzed three different antenna orientations for performance: locating the antenna on the top of the lens, the sides of the lens, and the side of the frame. Orienting the monopole on the side of the frame produced the highest peak SAR over 1 g of 1.520 W/kg, and orienting the antenna on the side of the lens produced the lowest one of 0.408 W/kg. The input power for these results was not specified. The side of the lens orientation also resulted in the highest gain of the three at 2.58 dBi. Using a scanning patch array to realize smart glasses for 60 GHz operation, Hong and Choi [2018] found that integrating a full ground on the bottom plane of the array allowed for nearly unchanged operation in the presence of a human head model compared to the no-head model, in spite of tissue's high absorbance of EM energy at such a high frequency. Using the ICNIRP power density guidelines for millimeter-wave EM exposure ($<10\ W/m^2$) [Hong and Choi, 2018], the glasses exhibited a peak power density of $9.48\ W/m^2$ with an input power of 1.4 W (350 mW per port), corresponding to a peak SAR of 4.8 W/kg.

Health tracking/medical device operation is also a common wearable device function. Lee and Jung [2015] presented a radiation-pattern-reconfigurable antenna, consisting of a monopole and loop antenna contacting a pole top-loaded with a monopole, designed to integrate into a Fitbit Flex smartwatch band. Operating at 2.4 GHz, the antenna exhibited peak SAR over 1 g ranging from 0.94 to 1.11 W/kg, depending on the scan angle. Their antenna exhibits a 40–50% improvement in efficiency over the Flex's integrated antenna. Ruaro et al. [2016] designed a wearable shell antenna for 2.4 GHz operation designed to work as a hearing aid. The SAR over 1 g is modeled at 0.05 mW, as this device operates with a low-duty cycle, and is 0.0007 W/kg. SAR was also modeled for an input power of 0.01 W, the maximum input for Bluetooth Low Energy (BLE) operation, with a resulting value within safe levels of 1.30 W/kg. Popovic et al. [2014] used SAR calculations to quantify how much power the body emits to implement a non-invasive wireless core-body sensing thermometer. Based on these simulations, the conformal thermometer, operating at 1.4 and 2.7 GHz, is able to measure temperatures up to several centimeters into the body with an error less than 0.5 K (0.5°C).

IMPLANTS

Overview of Implantable Antenna Design

As implantable antennas are designed to be located inside the body, additional challenges beyond those of wearable antennas must be taken into account. The dimensions of an implanted antenna should be reduced as much as possible in order to increase the likelihood of integrating within the body, so miniaturization techniques play an important role in design. For example, Zhang et al. [2018] designed a circular patch antenna for operation at 915 MHz of size $\pi \times (4.7)^2 \times 1.27\ mm^2$. The antenna size normally required for operation at this frequency was decreased by cutting various slot configurations to increase the effective current path length and by implementing a shorting pin to also increase the antenna's effective size. Additional miniaturization techniques include using high permittivity dielectric substrates and superstrates and vertically stacking radiating patches [Kiourti and Nikita, 2012a]. The environment of the antenna itself assists with miniaturization of the antenna—the high permittivity of body tissues decreases the effective wavelength—but also introduces loss into the communication path with external devices. This path loss presents a tradeoff, as high gain becomes an important design parameter but often decreases as an antenna is miniaturized. Lesnik et al. [2018] managed this tradeoff by using a partial miniaturization technique. They designed a miniature implantable planar dipole antenna of volume $20\ mm^3$ by meandering the antenna arms to increase the current path length, which normally decreases gain, while maintaining a moderate peak realized gain of -23.7 dBi by meandering only the ends of the arms. Additionally, as the tissue environment varies from person to person and over time within the same person, wider bandwidths are generally more favorable to account for detuning of the antenna. However, miniaturization can also decrease bandwidth. See et al. [2015] countered this decrease by using a differential loop-fed patch antenna, which excites an antiphase mode via proximity coupling, doubling the expected bandwidth.

Another important consideration for implanted antennas is biocompatibility, which as with miniaturization, is to ensure integration with the body. One

method is to use a biocompatible substrate, such as alumina, which Bakogianni and Koulouridis [2016] suggested for their planar dipole. Blauert et al. [2018] use another common method of coating the antenna with a biocompatible polymer, such as polydimethylsiloxane (PDMS), for their dual-band patch antenna.

Dosimetry for Implantable Antennas

SAR values. Similar to SAR values acquired for wearable antennas, different groups use different phantoms, input powers, etc. to determine SAR, but the safe limits as outlined by the IEEE, FCC, and ICNIRP remain the same. An additional degree of freedom when determining SAR for implantable antennas is how deep within the body the device is located. Various antennas, their corresponding test setups, and their worst-case scenario SAR values are shown in Table 3.

Of the three PIFA antennas reported in Table 3, Liu et al.'s [2014] and Duan et al.'s [2014] both operate around 2.4 GHz and in similar phantom setups, but Liu et al.'s PIFA, the smaller of the two, exhibits a much lower SAR value. Duan et al.'s dual-band PIFA additionally exhibits a higher SAR at the higher frequency band. Li et al.'s [2015] PIFA is comparable with the lower frequency band's operation, size, and phantom setup of Duan et al.'s [2014] PIFA, but Li et al.'s PIFA, which uses a different geometry, exhibits a higher SAR. Of the two circularly polarized patch antennas in Table 3, which are similar in phantom setup including implant depth, the patch operating at higher frequencies exhibits a reduced SAR.

As with wearable antennas, SAR values are dependent on the environment in which the antenna is operating, as well as the antenna type and geometry, with the addition of a variable depth of implantation; thus, conclusions derived from reviewing the literature are application-specific. The following sections summarize such findings wherever possible and to the most extent possible.

SAR and field distributions. The safety and performance of an implantable antenna are related through SAR. As with wearable antennas, the SAR for implantable antennas can be determined experimentally by probing the electric field in a phantom in which the antenna is implanted. By using the DASY3 automated SAR measurement system, Scarpello et al. [2011] were able to determine that their flexible folded slot dipole antenna designed to operate at 2.45 GHz in the body satisfies the 1- and 10-g SAR limits, exhibiting SAR of 0.079 and 0.032 W/kg, respectively.

Near-field loss is associated with current distribution on the antenna as well as SAR, so increased near-field loss is associated with higher SAR values. Das and Yoo [2017] designed a ground-slotted patch antenna for operation at 402–405 MHz, 1.45–1.6 GHz, and 2.4–2.45 GHz and proceeded to optimize their antenna via the current distribution. As shown in Figure 6, the placement and T-shape of the slot antenna allows the current to flow in such a way to enable multiband operation, and, as specifically shown in Figures 6e and f, to increase gain resulting in less power dissipated in the tissue. As a result, the maximum allowable input power for SAR averaged over 1 and 10 g is 3.9 and 31.9 mW, respectively.

Liu et al. [2016] analyzed the current and electric field distribution to determine how their test setup was affecting the performance of their on-chip dipole antenna with spiral arms. Analyses of the antenna's current without the test setup showed that adjacent arms are in-phase, increasing self-inductance, and SAR analysis of just the antenna resulted in a maximum allowable input power of 11.9 and 148.9 mW for 1 and 10 g averages, respectively. The antenna was designed with ground-signal-ground-signal-ground (GSGSG) pads, the test probe for which is not feasible for use in a phantom, so wire-bonding was used as a chip-to-SMA transition for experimental data collection. With this test setup, the antenna exhibited an increased coupling coefficient compared with simulations. Analysis of the electric field distribution of a simulation including the wire-bonding showed that this transition structure was also contributing to radiation.

Bahrami et al. [2015] analyzed the electric field distribution to determine safety of their monopole patch antenna as well as optimal placement and radiation characteristics. By visualizing the electric field, they determined the near/far-field boundary and determined that a radius of 7 mm from the implanted antenna is the optimal location within this region to place a receiver. They also determined that placement of the antenna below and above the skull were both limited to the same maximum input power of 2.2 mW for SAR averaged over 1 g, though the SAR in the bone limited the under-bone input power, whereas the SAR in the skin limited the under-skin input power.

Certain types of antennas generally perform better in terms of electric field distribution and SAR. Manteghi and Ibraheem [2014] found that magnetic antennas, such as loops, are advantageous as compared with electric field antennas, such as dipoles and patches, with regard to power dissipated in the near field. In terms of variations in phantoms, Kiourti and Nikita [2013] found that antenna performance is primarily affected by the head phantom anatomy,

TABLE 3. Comparison of Various Implantable Antennas and Their Corresponding Specific Absorption Rate (SAR) Values

Source	Antenna design	Size	Operation frequency	Input power for SAR calculation (mW)	$SAR_{1\,g}$ (W/kg)	$SAR_{10\,g}$ (W/kg)	SAR normalized to 1 W input power, 1 g; 10 g	Phantom type and distance to antenna
Liu et al. [2014]	PIFA	$4 \times 8\,mm^2$	2.45 GHz	1,000	0.142	0.0463	0.142; 0.0463	Voxel body chest model
Liu et al. [2017]	Circularly polarized patch	$8.5 \times 8.5 \times 1.27\,mm^3$	2.32–2.62 GHz	7.59	1.6	–	211; –	Three-layer tissue model (4 mm skin, 4 mm fat, 32 mm muscle) antenna 2–4 mm below surface
Zhang et al. [2018]	Circularly polarized patch	$\pi \times 4.7^2\ 1.27\,mm^3$	915 MHz	1,000	778	–	778; –	Three-layer tissue model (4 mm skin, 4 mm fat, 36 mm muscle), $80 \times 80\,mm^2$, antenna 2 mm below surface
Xiao and Li [2014]	Semicircular PIFA	$151\,mm^3$	402–405 MHz	1,000	606	–	606; –	One-layer tissue model (skin), $99 \times 99 \times 50\,mm^3$, antenna 3 mm below surface
Felicio et al. [2016]	Slotted circular patch	$7.85^2 \times \pi\,mm^2$	1.4–4.2 GHz	2.22	1.6	–	721; –	Three-layer tissue model (1 mm skin, 1 mm fat, 40 mm muscle), $100 \times 100\,mm^2$, antenna 3 mm below surface
Lesnik et al. [2018]	Meandered dipole	$20\,mm^3$	401–406 MHz	1,000	219	47	219; 47	Cylindrical three-layer tissue model (2.5 mm skin, 20 mm muscle, 12.5 mm bone), 100 mm long, antenna 2 mm below surface
Duan et al. [2014]	PIFA	$13.2 \times 15.8 \times 0.635\,mm^3$	402–405 MHz, 2.4–2.5 GHz	1,000	–	85.2/77.8	–; 85.2/77.8	Voxel body chest model
See et al. [2015]	Loop-fed patch	$24 \times 10 \times 0.95\,mm^3$	4.1–4.5 GHz	28	1.6	–	57; –	Three-layer tissue model (5 mm skin, 2.5 mm tendon, 5 mm cortical bone), $125 \times 125\ mm^2$, antenna 2 mm below surface
Bakogianni and Koulouridis [2016]	L-shaped Planar dipole	$18.1\,mm^3$	401–406 MHz	1,000	426.5	96.8	426.5; 96.8	One-layer tissue model (skin), $150 \times 150 \times 150\,mm^3$
Blauert et al. [2018]	Meandered patch	$7.7 \times 6.9 \times 1.52\,mm^3$	2.4/4.8 GHz	2.80	1.6	–	571; –	Three-layer tissue model (2 mm skin, 8 mm fat, 10 mm muscle), $60 \times 60\,mm^2$, antenna 2 mm below surface

(*Continued*)

TABLE 3. *Continued*

Source	Antenna design	Size	Operation frequency	Input power for SAR calculation (mW)	$SAR_{1\,g}$ (W/kg)	$SAR_{10\,g}$ (W/kg)	SAR normalized to 1 W input power, 1 g; 10 g	Phantom type and distance to antenna
Li et al. [2015]	PIFA	$12.5 \times 12.5 \times 1.27$ mm^3	401–406 MHz	1,000	192.59	36.23	192.59; 36.23	Voxel body model
Li et al. [2017]	Annular ring	120.69 mm^3	2.4–2.48 GHz	1,000	733.5	–	733.5	One-layer tissue model (skin), $>90 \times 90 \times 24$ mm^3, antenna 4 mm below surface
Tsai et al. [2016]	Sigma shaped monopole	80 mm^3	350–680 MHz	1,000	230	–	230	One-layer tissue model (muscle), $70 \times 70 \times 70$ mm^3, antenna placed at the center

PIFA = planar inverted-F antenna.

more so than tissue anatomy and EM characteristics. In studying various layered head models with tissues of varying EM characteristics, they found that the maximum-allowed input power for a generic patch antenna varied by less than 3.7% at 403.5 MHz.

Thermal distribution. As mentioned previously when discussing wearable antennas, the induced temperature change, rather than the power density itself, is what poses the greatest risk to those exposed to RF radiation. Kyriakou et al. [2012] studied a basic radiator—an insulated wire with uninsulated tips—to determine if the SAR values associated with a tissue temperature increase of 1°C align with the safety limits set by various national and international organizations for a range of 10–1,000 MHz. Using both simulations and experiments, they determined that the square of the electric field tangential to the wire resulting in a temperature increase of 1°C was 1,500 times less than the current basic restrictions on local SAR as given by the 1998 ICNIRP and IEEE C95.1–2005 guidelines. They did note that their setup made some simplifications, such as not accounting for blood perfusion, and thus may overestimate the values normally associated with such exposure. In more accurate simulations, however, similar exposure levels were observed, and therefore, Kyriakou et al. conclude that the SAR regulations may not be sufficient for all implant situations.

To ensure the safety of a retinal prosthesis, Gosalia et al. [2004] evaluated both the induced SAR and corresponding temperature increase associated with an exterior extraocular and an implanted intraocular unit connected wirelessly. Normal wireless operation of the device was well within safe SAR limits (0.021 W/kg averaged over 1 g at 10 MHz), so the implanted intraocular unit was considered as the sole heat source in their simulations. Using a 3D model, they found that the maximum temperature increase of 0.82°C occurred on the insulation layer of the implanted device, followed by the vitreous cavity (0.26°C maximum) and the retina (0.12°C maximum). They noted that anterior placement of the implant (between the eye's ciliary muscles) exhibited less heating than center placement (middle of the vitreous cavity), aside from in the vitreous cavity itself.

With the increasing prominence of implanted devices, Tang et al. [2005] studied communication scheduling on the heating effects of using multiple devices or nodes routed through a main communication device. They developed a genetic algorithm that solves a simplified version of Pennes' bioheat equation to determine the tissue temperature increase

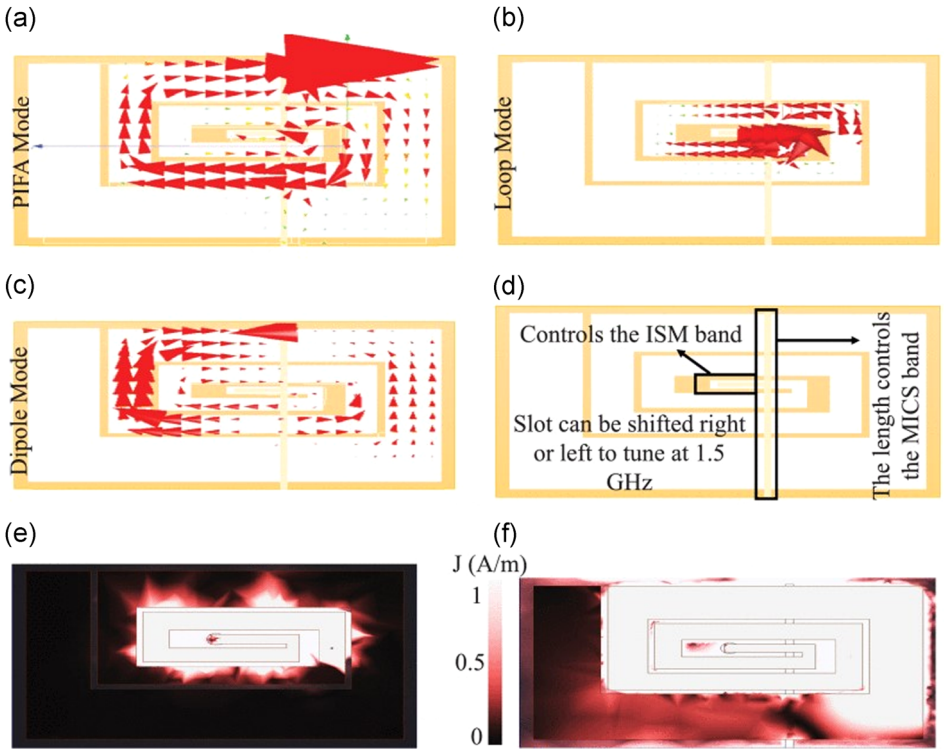

Fig. 6. Analyzing current flow on an antenna can better inform the safety and efficiency of the design. For example, the addition of a well-placed slot on this antenna increased the gain, subsequently decreasing specific absorption rate. Current flow of the ground-slotted patch antenna at (**a**) 405 MHz (**b**) 1.5 GHz (**c**) 2.45 GHz. (**d**) Depiction of how the antenna radiates at the given frequencies, where ISM stands for the Industrial, Scientific, and Medical frequency bands and MICS stands for the Medical Implant Communication Service frequency band (currently known as the Medical Device Radiocommunications Service or MedRadio band). Current distribution of the patch antenna (**e**) without the slot and (**f**) with the slot [Das and Yoo, 2017]. PIFA = planar inverted-F antenna.

at a given node's location. The algorithm then prioritizes the next node to communicate based on this temperature increase and the node's location and leadership history. They found that for a 10-node test, their algorithm exhibited a smaller temperature increase (0.0934 vs. 0.1051°C) and smaller standard deviation (0.0062°C vs. 0.0117°C) than the worst possible sequence, indicating that implementation of such algorithms is important for the safe operation of multiple implanted devices.

Thermal heating of implanted devices can also be advantageous. Reeves et al. [2002] investigated the use of helical antennas to treat Barrett's oesophagus. They studied the use of helical antennas as flexible endoscopes for the ablation of precancerous and cancerous masses. Using a muscle equivalent phantom and IR cameras, Reeves et al. designed a group of helical antennas of varying lengths and coil densities operating at 915 MHz and exhibiting less than a 20% temperature decrease across the antenna's length with a steep temperature decrease at the end. These criteria were selected to ensure that the desired area of the body, and only that area, is heated. In analyzing the effect of coil density, a 25-mm antenna with the highest density coil spacing tested ($S = 2.3$ mm) exhibited two temperature peaks along the length of the antenna. The 50% SAR falloff along the length of the antenna ranged from 1 to 4 mm from the end of the antenna. The 50% radial SAR falloff ranged from 2.5 to 3.2 mm from the surface of the antennas with the maximum SAR ranging from 42.9 ± 5.1 W/kg/W_{input} to 74.3 ± 4.7 W/kg/W_{input}, where W_{input} is the input power to the antenna. SAR was calculated by multiplying specific heat of the phantom used (2,940 J/kg/°C) by the maximum recorded temperature increase and then by normalizing to 1 W of input power.

Reducing SAR Levels

Similar to wearable antennas, metamaterials may also be employed to reduce the SAR of

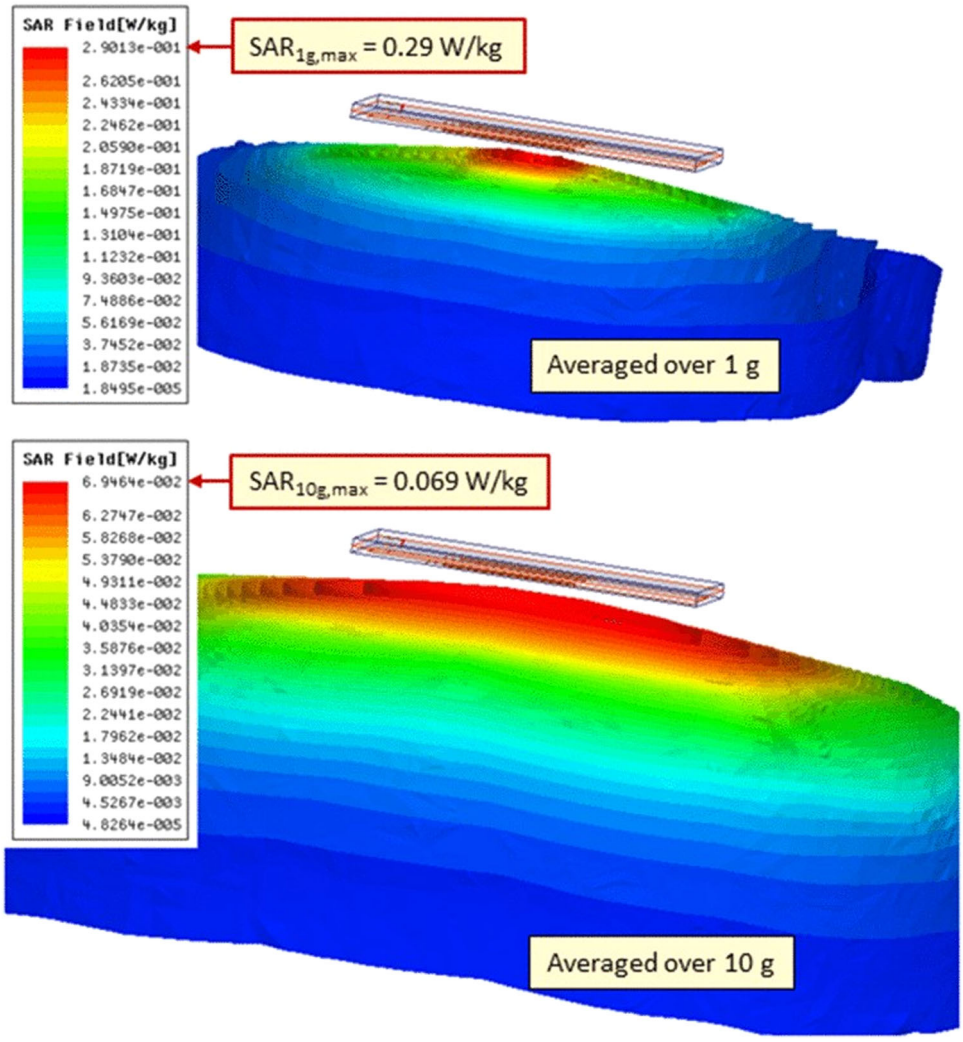

Fig. 7. Specific absorption rate (SAR) distribution of a fully passive, wireless neural recording system, where the maximum expected transmit power results in SAR levels well within safety limits [Lee et al., 2017].

implantable antennas. Alrawashdeh et al. [2015] used CSRRs to decrease the SAR of their flexible implantable loop antenna with a surface area of 30×15 mm. The loop was designed with a wide bandwidth to cover parts of both the MedRadio and ISM frequency bands. The maximum SAR averaged over 1 g was 118 W/kg with 1 W of input power, indicating the maximum input power to stay within 1.6 W/kg of exposure is 11.3 dBm (13.56 mW) as simulated in muscle tissue. The CSRRs decrease the antenna's electric near field, thus decreasing SAR below that of the loop antenna alone—without the CSRRs, SAR is 189 W/kg. By decreasing the near field, the CSRRs also effectively increase the radiation efficiency and gain.

Tsai et al. [2016] focused on uniformly distributing current across the surface of the antenna to reduce SAR, using a C-shaped ground plane for a monopole antenna of volume 80 mm^3. The flexible antenna exhibited a maximum SAR averaged over 1 g of tissue of 230 W/kg for a 1 W input power. Kiourti and Nikita [2012b] also focused on current distribution across the antenna to decrease SAR. By increasing the operation frequency of a PIFA without proportionally decreasing the physical size, they produced an antenna operating at 915 MHz that was the same size as an antenna operating at 402 MHz but with a decreased maximum SAR. The 915 MHz PIFA SAR averaged over 1 g was 294.86 W/kg compared with 324.74 W/kg for the 402 MHz antenna, each calculated for 1 W of input power.

Dosimetry for Integrated Implantable Devices

Many implantable devices are designed for medical applications. One of the more common implants is a cardiac pacemaker, and envisioning a future pacemaker with Wi-Fi capability, Kovar et al. [2017] analyzed the safety of such a device. When simulating a 5 GHz, 28.6 mm long dipole antenna integrated with a pacemaker, they found that maximum SAR over 10 g was above the 2 W/kg limit for certain antenna locations, which they reported not only affects the user but also may affect pacemaker function.

Another popular application for implantable devices is intraocular pressure (IOP) monitoring systems for glaucoma. Chiou et al. [2016] designed a reader and tag system of loop antennas with the tag integrated into a contact lens for such monitoring and the reader integrated into a pair of glasses. The operation principle is based on that of a radiofrequency identification (RFID) system, where the interrogator is designed to wirelessly transmit power to and read out the pressure data from the implant. Using a seven-tissue eye model, SAR simulations showed that power transmission levels considered safe by the FCC 1.6 W/kg limit are 18 dBm at a loop separation of 10 mm and 24 dBm at a loop separation of 20 mm at 925 MHz. Donida et al. [2015] also designed an IOP sensor for a contact lens, likewise using an external reader integrated into glasses. With a coil separation of 40 mm and an input power of 1.4 mW (the power necessary for device operation), they found that maximum local SAR was 0.006 W/kg. Schaumburg and Guarnieri [2017] designed a wireless microvalve to treat glaucoma. The external interrogator provides power via a 10-turn rectangular coil to the internal unit using a nine-turn octagonal coil. The device is designed to operate at 13.56 MHz. In a 10-tissue anatomical head model, the SAR averaged over 10 g peaked at the eyebrow with a maximum value of 0.024 W/kg produced via a 1.24 ampere-turn operation current for the external antenna—the minimum necessary for the device to operate.

RFID-based systems are also commonly used for brain interfaces. Lee et al. [2017] proposed a fully passive neurosensing system in which the external unit interrogates the internal unit with a 2.4 GHz signal to collect backscattered neural signals modulated with a 4.8 GHz carrier signal. Unlike the previously mentioned systems, theirs utilizes patch antennas as opposed to loops. The peak SAR of the system with the implant located 1 mm below the skin and the interrogator 1 mm above the skin was 0.29 W/kg averaged over 1 g and 0.069 W/kg averaged over 10 g. The input power to the external antenna was 6 dBm. The SAR distribution is shown in Figure 7, and as with the other SAR distributions presented, the maximum SAR is found directly below the antenna in the skin layer. Song and Rahmat-Samii [2017] implemented a similar device using coils with an external segmented loop and an internal 3D cubic loop. The maximum SAR at 400 GHz of the device was produced on top of the skin and limited the input power to 18 dBm.

CONCLUSION

This paper presents a comprehensive overview of the dosimetry aspects relevant to wearable and implantable antennas. Placing radiators close to or within the body poses challenges for both radiation efficiency and device safety. The primary indicator of dosimetry for such increasingly prevalent devices, SAR, manifests as a temperature increase within body tissues. When SAR peaks outside of the safe limits outlined by the IEEE, ICNIRP, and FCC, damage to the surrounding tissues, usually those located closest to the device, can occur. As such, designers of wearable and implantable devices are taking steps to reduce SAR levels while maintaining the radiation characteristics of the antenna. Both designers of wearable devices and designers of implantable devices share many of the methods used to reduce SAR, such as metamaterials and other ground plane alterations, and all methods seek to reduce peak areas of the electric field. As these devices continue to grow in popularity, designers must not only consider the safety of their own device but also the combined safety of the other devices that may be implemented on/in the same person.

REFERENCES

Abirami BS, Sundarsingh EF. 2017. EBG-backed flexible printed Yagi–Uda antenna for on-body communication. IEEE Trans Antennas Propag 65:3762–3765.

Agarwal K, Guo Y-X, Salam B. 2016. Wearable AMC backed near-endfire antenna for on-body communications on latex substrate. IEEE Trans Compon Packag Manuf Technol 6:346–358.

Agneessens S, Lemey S, Vervust T, Rogier H. 2015. Wearable, small, and robust: The circular quarter-mode textile antenna. IEEE Antennas Wirel Propag Lett 14:1482–1485.

Alharbi S, Chaudhari S, Inshaar A, Shah H, Zou C, Harne RL, Kiourti A. 2018. E-textile origami dipole antennas with graded embroidery for adaptive RF performance. IEEE Antennas Wirel Propag Lett 17:2218–2222.

Alkhamis R, Wigle J, Song H. 2017. Global positioning system and distress signal frequency wrist wearable dual-band antenna. Microw Opt Technol Lett 59:2057–2064.

Alrawashdeh RS, Huang Yi, Kod M, Abu Bakar Sajak A. 2015. A broadband flexible implantable loop antenna with

complementary split ring resonators. IEEE Antennas Wirel Propag Lett 14:1506–1509.
Amar ABen, Kouki AB, Cao H. 2015. Power approaches for implantable medical devices. *Sensors (Basel)*, 15. pp 28889–28914.
Anguera J, Andújar A, Picher C, González L, Puente C, Kahng S. 2012. Behavior of several antenna topologies near the human head at the 2.4-2.5 GHz band. Microw Opt Technol Lett 54:1911–1916.
Ashyap AYI, Zainal Abidin Z, Dahlan SH, Majid HA, Shah SM, Kamarudin MR, Alomainy A. 2017. Compact and low-profile textile EBG-based antenna for wearable medical applications. IEEE Antennas Wirel Propag Lett 16:2550–2553.
Augustine R, Alves T, Sarrebourse T, Poussot B, Mathew KT, Laheurte J-M. 2010. Polymeric ferrite sheets for SAR reduction of wearable antennas. Electron Lett 46:197.
Bahrami H, Mirbozorgi SA, Rusch LA, Gosselin B. 2015. Biological channel modeling and implantable UWB antenna design for neural recording systems. IEEE Trans Biomed Eng 62:88–98.
Bakogianni S, Koulouridis S. 2016. An implantable planar dipole antenna for wireless MedRadio-band biotelemetry devices. IEEE Antennas Wirel Propag Lett 15:234–237.
Bandodkar AJ. 2017. Review—wearable biofuel cells: Past, present and future. J Electrochem Soc 164:H3007–H3014.
Bergmann JHM, Chandaria V, McGregor A. 2012. Wearable and implantable sensors: The patient's perspective. Sensors (Basel) 12:16695–16709.
Bhattacharjee S, Mitra M, Chaudhuri SRB. 2017. An effective SAR reduction technique of a compact meander line antenna for wearable applications. Prog Electromagn Res 55:143–152.
Blauert J, Kang Y-S, Kiourti A. 2018. In vivo testing of a miniature 2.4/4.8 GHz implantable antenna in postmortem human subject. IEEE Antennas Wirel Propag Lett 17:2334–2338.
Blauert J, Kiourti A. 2018. Bio-matched horn: A novel 1-9 GHz on-body antenna for low-loss biomedical telemetry with implants. IEEE Trans Antennas Propag 67:5054–5062.
Chen Y-S, Ku T-Y. 2016. A low-profile wearable antenna using a miniature high impedance surface for smartwatch applications. IEEE Antennas Wirel Propag Lett 15:1144–1147.
Chiou J-C, Hsu S-H, Liao Y-T, Huang Y-C, Yeh G-T, Kuei C-K, Dai K-S. 2016. Toward a wirelessly powered on-lens intraocular pressure monitoring system. IEEE Biomed Heal Informatics 20:1216–1224.
Chou C-K, D'Andrea JA. 2003. Reviews of effects of RF fields on various aspects of human health: introduction. Bioelectromagnetics 24:S5–S6.
Chou CK, Bassen H, Osepchuk J, Balzano Q, Petersen R, Meltz M, Cleveland R, Lin JC, Heynick L. 1996. Radio frequency electromagnetic exposure: Tutorial review on experimental dosimetry. Bioelectromagnetics 17:195–208.
Das R, Yoo H. 2017. A multiband antenna associating wireless monitoring and nonleaky wireless power transfer system for biomedical implants. IEEE Trans Microw Theory Tech 65:2485–2495.
Donida A, Di Dato G, Cunzolo P, Sala M, Piffaretti F, Orsatti P, Barrettino D. 2015. A circadian and cardiac intraocular pressure sensor for smart implantable lens. IEEE Trans Biomed Circuits Syst 9:777–789.
Duan Z, Guo Y-X, Je M, Kwong D-L. 2014. Design and in vitro test of a differentially fed dual-band implantable antenna operating at MICS and ISM bands. IEEE Trans Antennas Propag 62:2430–2439.
FCC OET. 1997. Evaluating compliance with FCC guidelines for human exposure to radio frequency electromagnetic fields. Bulletin 65. Washington, DC: FCC OET.
Felicio JM, Fernandes CA, Costa JR. 2016. Wideband implantable antenna for body-area high data rate impulse radio communication. IEEE Trans Antennas Propag 64:1932–1940.
Fernández-Garcia R, Gil I. 2017. An alternative wearable tracking system based on a low-power wide-area network. Sensors 17:592.
Fernandez M, Espinosa HG, Thiel DV, Arrinda A. 2018. Wearable slot antenna at 2.45 GHz for off-body radiation: Analysis of efficiency, frequency shift, and body absorption. Bioelectromagnetics 39:25–34.
Gao G, Hu B, Wang S, Yang C. 2018. Wearable planar inverted-F antenna with stable characteristic and low specific absorption rate. Microw Opt Technol Lett 60:876–882.
Gosalia K, Weiland J, Humayun M, Lazzi G. 2004. Thermal elevation in the human eye and head due to the operation of a retinal prosthesis. IEEE Trans Biomed Eng 51:1469–1477.
Grant H, Heirman D, Kuriger G, Ravindran MM. 2004. In vitro study of the electromagnetic interaction between wireless phones and an implantable neural stimulator. Bioelectromagnetics 25:356–361.
Gwechenberger M, Rauscha F, Stix G, Schmid G, Strametz-Juranek J. 2006. Interference of programmed electromagnetic stimulation with pacemakers and automatic implantable cardioverter defibrillators. Bioelectromagnetics 27:365–377.
Hinchet R, Kim S-W. 2015. Wearable and implantable mechanical energy harvesters for self-powered biomedical systems. ACS Nano 9:7742–7745.
Hong S-E, Lee A-K, Kwon J-H, Pack J-K. 2016a. Numerical compliance testing of human exposure to electromagnetic radiation from smart-watches. Phys Med Biol 61:6975–6992.
Hong S, Kang SH, Kim Y, Jung CW. 2016b. Transparent and flexible antenna for wearable glasses applications. IEEE Trans Antennas Propag 64:2797–2804.
Hong Y, Choi J. 2018. 60 GHz patch antenna array with parasitic elements for smart glasses. IEEE Antennas Wirel Propag Lett 17:1252–1256.
International Commission on Non-Ionizing Radiation Protection. 1998. ICNIRP guidelines for limiting exposure to time-varying, electric, magnetic, and electromagnetic fields (up to 300 GHz). Health Phys 74:494–522.
IEEE Standard C95.1-2005. 2005. IEEE standard for safety levels with respect to human exposure to radio frequency electromagnetic fields, 3 kHz to 300 GHz. New York, NY: IEEE.
Jiang ZH, Brocker DE, Sieber PE, Werner DH. 2014. A compact, low-profile metasurface-enabled antenna for wearable medical body-area network devices. IEEE Trans Antennas Propag 62:4021–4030.
Jiang ZH, Gregory MD, Werner DH. 2016. Design and experimental investigation of a compact circularly polarized integrated filtering antenna for wearable biotelemetric devices. IEEE Trans Biomed Circuits Syst 10:328–338.
Karthik V, Rao T. 2017. Investigations on SAR and thermal effects of a body wearable microstrip antenna. Wirel Pers Commun 96:3385–3401.
Karthik V, Rao TR. 2018. SAR investigations on the exposure compliance of wearable wireless devices using infrared thermography. Bioelectromagnetics 39:451–459.
Kiourti A. 2018. RFID antennas for body-area applications: From wearables to implants. IEEE Antennas Propag Mag 60: 14–25.

Kiourti A, Nikita KS. 2012a. A review of implantable patch antennas for biomedical telemetry: Challenges and solutions [wireless corner]. IEEE Antennas Propag Mag 54:210–228.

Kiourti A, Nikita KS. 2012b. Miniature scalp-implantable antennas for telemetry in the MICS and ISM bands: Design, safety considerations and link budget analysis. IEEE Trans Antennas Propag 60:3568–3575.

Kiourti A, Nikita KS. 2013. Numerical assessment of the performance of a scalp-implantable antenna: Effects of head anatomy and dielectric parameters. Bioelectromagnetics 34:167–179.

Kiourti A, Nikita KS. 2017. A review of in-body biotelemetry devices: Implantables, ingestibles, and injectables. IEEE Trans Biomed Eng 64:1422–1430.

Kiourti A, Psathas KA, Nikita KS. 2014. Implantable and ingestible medical devices with wireless telemetry functionalities: A review of current status and challenges. Bioelectromagnetics 35:1–15.

Klemm M, Troester G. 2006. EM energy absorption in the human body tissues due to UWB antennas. Prog Electromagn Res PIER 62:261–280.

Kovar S, Spano I, Gatto G, Valouch J, Adamek M. 2017. SAR evaluation of wireless antenna on implanted cardiac pacemaker. J Electromagn Waves Appl 31:627–635.

Koydemir HC, Ozcan A. 2018. Wearable and implantable sensors for biomedical applications. Annu Rev Anal Chem 11:127–146.

Kwak S, il, Sim D-U, Kwon JH, Yoon YJ. 2017. Design of PIFA with metamaterials for body-SAR reduction in wearable applications. IEEE Trans Electromagn Compat 59: 297–300.

Kyriakou A, Christ A, Neufeld E, Kuster N. 2012. Local tissue temperature increase of a generic implant compared to the basic restrictions defined in safety guidelines. Bioelectromagnetics 33:366–374.

Lee CM, Jung CW. 2015. Radiation-pattern-reconfigurable antenna using monopole-loop for Fitbit flex wristband. IEEE Antennas Wirel Propag Lett 14:269–272.

Lee CWL, Kiourti A, Volakis JL. 2017. Miniaturized fully passive brain implant for wireless neuropotential acquisition. IEEE Antennas Wirel Propag Lett 16:645–648.

Lesnik R, Verhovski N, Mizrachi I, Milgrom B, Haridim M. 2018. Gain enhancement of a compact implantable dipole for biomedical applications. IEEE Antennas Wirel Propag Lett 17:1778–1782.

Li H, Guo Y-X, Liu C, Xiao S, Li L. 2015. A miniature-implantable antenna for medradio-band biomedical telemetry. IEEE Antennas Wirel Propag Lett 14:1176–1179.

Li R, Guo Y-X, Zhang B, Du G. 2017. A miniaturized circularly polarized implantable annular-ring antenna. IEEE Antennas Wirel Propag Lett 16:2566–2569.

Liu C, Guo Y-X, Liu X, Xiao S. 2016. An integrated on-chip implantable antenna in CMOS technology for biomedical applications. IEEE Trans Antennas Propag 64:1167–1172.

Liu C, Guo Y-X, Sun H, Xiao S. 2014. Design and safety considerations of an implantable rectenna for far-field wireless power transfer. IEEE Trans Antennas Propag 62:5798–5806.

Liu XY, Wu ZT, Fan Y, Tentzeris EM. 2017. A miniaturized CSRR loaded wide-beamwidth circularly polarized implantable antenna for subcutaneous real-time glucose monitoring. IEEE Antennas Wirel Propag Lett 16: 577–580.

Mandal D, Pattnaik SS. 2018. Quad-band wearable slot antenna with low SAR values for 1.8 GHz DCS, 2.4 GHz WLAN and 3.6/5.5 GHz WiMAX applications. Prog Electromagn Res 81:163–182.

Manoufali M, Bialkowski K, Mohammed BJ, Mills PC, Abbosh A. 2018. Near-field inductive-coupling link to power a three-dimensional millimeter-size antenna for brain implantable medical devices. IEEE Trans Biomed Eng 65:4–14.

Manteghi M, Ibraheem AAY. 2014. On the study of the near-fields of electric and magnetic small antennas in lossy media. IEEE Trans Antennas Propag 62:6491–6495.

Martínez-Búrdalo M, Martín A, Sanchis A, Villar R. 2009. FDTD assessment of human exposure to electromagnetic fields from WiFi and bluetooth devices in some operating situations. Bioelectromagnetics 30:142–151.

Polikov VS, Tresco PA, Reichert WM. 2005. Invited review response of brain tissue to chronically implanted neural electrodes. J Neurosci Methods 148:1–18.

Popovic Z, Momenroodaki P, Scheeler R. 2014. Toward wearable wireless thermometers for internal body temperature measurements. IEEE Commun Mag 52:118–125.

Reeves J, Birch M, Munro K, Collier R. 2002. Investigation into the thermal distribution of microwave helical antennas designed for the treatment of Barrett's oesophagus. Phys Med Biol 47:3557–3564.

Ruaro A, Thaysen J, Jakobsen KB. 2016. Wearable shell antenna for 2.4 GHz hearing instruments. IEEE Trans Antennas Propag 64:2127–2135.

Saeed SM, Balanis CA, Birtcher CR, Durgun AC, Shaman HN. 2017. Wearable flexible reconfigurable antenna integrated with artificial magnetic conductor. IEEE Antennas Wirel Propag Lett 16:2396–2399.

Scarpello ML, Kazani I, Hertleer C, Hendrik R, Dries VG. 2012. Stability and efficiency of screen printed wearable and washable antennas. IEEE Trans Antennas Propag 11: 838–841.

Scarpello ML, Kurup D, Rogier H, Vande Ginste D, Axisa F, Vanfleteren J, Joseph W, Martens L, Vermeeren G. 2011. Design of an implantable slot dipole conformal flexible antenna for biomedical applications. IEEE Trans Antennas Propag 59:3556–3564.

Schaumburg F, Guarnieri FA. 2017. Assessment of thermal effects in a model of the human head implanted with a wireless active microvalve for the treatment of glaucoma creating a filtering bleb. Phys Med Biol 62:N191–N203.

See TSP, Qing X, Liu W, Chen ZN. 2015. A wideband ultra-thin differential loop-fed patch antenna for head implants. IEEE Trans Antennas Propag 63:3244–3248.

Shrivastava P, Rao TR. 2017. Investigations of SAR distributions and temperature elevation on human body at 60 GHz with corrugated antipodal linear tapered slot antenna. Prog Electromagn Res 59:111–121.

Song JK, Cho TH, Pan H, Song YM, Kim IS, Lee TH, Hwang SJ, Kim SJ. 2009. An electronic device for accelerating bone formation in tissues surrounding a dental implant. Bioelectromagnetics 30:374–384.

Song L, Rahmat-Samii Y. 2017. An end-to-end implanted brain–machine interface antenna system performance characterizations and development. IEEE Trans Antennas Propag 65:3399–3408.

Sundarsingh EF, Velan S, Kanagasabai M, Sarma AK, Raviteja C, Alsath MGN. 2014. Polygon-shaped slotted dual-band

antenna for wearable applications. IEEE Antennas Wirel Propag Lett 13:611–614.

Tang Q, Tummala N, Gupta SKS, Schwiebert L. 2005. Communication scheduling to minimize thermal effects of implanted biosensor networks in homogeneous tissue. IEEE Trans Biomed Eng 52:1285–1294.

Tong X, Liu C, Liu X, Guo H, Yang X. 2018. Switchable ON-/OFF-body antenna for 2.45 GHz WBAN applications. IEEE Trans Antennas Propag 66:967–971.

Trajkovikj J, Skrivervik AK. 2015. Diminishing SAR for wearable UHF antennas. IEEE Antennas Wirel Propag Lett 14: 1530–1533.

Tsai C-L, Chen K-W, Yang C-L. 2016. Implantable wideband low-specific-absorption-rate antenna on a thin flexible substrate. IEEE Antennas Wirel Propag Lett 15: 1048–1052.

Velan S, Sundarsingh EF, Kanagasabai M, Sarma AK, Raviteja C, Sivasamy R, Pakkathillam JK. 2015. Dual-band EBG integrated monopole antenna deploying fractal geometry for wearable applications. IEEE Antennas Wirel Propag Lett 14:249–252.

Wang H, Zhang Z, Li Y, Feng Z. 2013. A dual-resonant shorted patch antenna for wearable application in 430 MHz band. IEEE Trans Antennas Propag 61:6195–6200.

Wood AW, Karipidis K. 2017. Non-ionizing radiation protection: Summary of research and policy options. Hoboken, NJ: Wiley. pp 1–10.

Xiaomu H, Yan S, Vandenbosch GAE. 2017. Wearable button antenna for dual-band WLAN applications with combined on and off-body radiation patterns. IEEE Trans Antennas Propag 65:1384–1387.

Xiao S, Li R. 2014. Compact slotted semi-circular antenna for implantable medical devices. Electron Lett 50:1675–1677.

Yan S, Soh PJ, Vandenbosch GAE. 2015a. Compact all-textile dual-band antenna loaded with metamaterial-inspired structure. IEEE Antennas Wirel Propag Lett 14:1486–1489

Yan S, Soh PJ, Vandenbosch GAE. 2015b. Wearable dual-band magneto-electric dipole antenna for WBAN/WLAN applications. IEEE Trans Antennas Propag 63:4165–4169.

Yan S, Vandenbosch GAE. 2016. Radiation pattern-reconfigurable wearable antenna based on metamaterial structure. IEEE Antennas Wirel Propag Lett 15:1715–1718.

Yan S, Vandenbosch GAE. 2018. Design of wideband button antenna based on characteristic mode theory. IEEE Trans Biomed Circuits Syst 12:1383–1391.

Zhang J, Yan S, Vandenbosch GAE. 2017a. A miniature feeding network for aperture-coupled wearable antennas. IEEE Trans Antennas Propag 65:2650–2654.

Zhang XY, Wong H, Mo T, Cao YF. 2017b. Dual-band dual-mode button antenna for on-body and off-body communications. IEEE Trans Biomed Circuits Syst 11:933–941.

Zhang Y, Liu C, Liu X, Zhang K, Yang X. 2018. A wideband circularly polarized implantable antenna for 915 MHz ISM-band biotelemetry devices. IEEE Antennas Wirel Propag Lett 17:1473–1477.

Zhu S, Langley R. 2009. Dual-band wearable textile antenna on an EBG substrate. IEEE Trans Antennas Propag 57: 926–935.